The Formation of the First Star in the Universe

Tom Abel,[1,2] Greg L. Bryan,[3] Michael L. Norman[4]

We describe results from a fully self-consistent three-dimensional hydrodynamical simulation of the formation of one of the first stars in the Universe. In current models of structure formation, dark matter initially dominates, and pregalactic objects form because of gravitational instability from small initial density perturbations. As they assemble via hierarchical merging, primordial gas cools through ro-vibrational lines of hydrogen molecules and sinks to the center of the dark matter potential well. The high-redshift analog of a molecular cloud is formed. As the dense, central parts of the cold gas cloud become self-gravitating, a dense core of $\sim$100 $M_\odot$ (where $M_\odot$ is the mass of the Sun) undergoes rapid contraction. At particle number densities greater than 10^9 per cubic centimeter, a 1 $M_\odot$ protostellar core becomes fully molecular as a result of three-body H_2 formation. Contrary to analytical expectations, this process does not lead to renewed fragmentation and only one star is formed. The calculation is stopped when optical depth effects become important, leaving the final mass of the fully formed star somewhat uncertain. At this stage the protostar is accreting material very rapidly ($\sim10^{-2}$ $M_\odot$ year^{-1}). Radiative feedback from the star will not only halt its growth but also inhibit the formation of other stars in the same pregalactic object (at least until the first star ends its life, presumably as a supernova). We conclude that at most one massive ($M \gg 1$ $M_\odot$) metal-free star forms per pregalactic halo, consistent with recent abundance measurements of metal-poor galactic halo stars.

Chemical elements heavier than lithium are synthesized in stars. Such "metals" are observed at times when the Universe was only $\sim <10\%$ of its current age in the intergalactic medium (IGM) as absorption lines in quasar spectra [see (*1*) and references therein]. Hence, these heavy elements not only had to be synthesized but also released and distributed in the IGM within the first billion years. Only supernovae of sufficiently short-lived massive stars are known to provide such an enrichment mechanism. This leads to the prediction that the first generation of cosmic structures formed massive stars (although not necessarily only massive stars).

In the past 30 years, it has been argued that the first cosmological objects formed globular clusters (*2*), supermassive black holes (*3*), or even low-mass stars (*4*). This disagreement of theoretical studies might at first seem surprising. However, the first objects formed via the gravitational collapse of a thermally unstable reactive medium, which inhibits conclusive analytical calculations. The problem is particularly acute because the evolution of all other cosmological objects (and in particular the larger galaxies that follow) depends on the evolution of the first stars.

Nevertheless, in comparison to present-day star formation, the physics of the formation of the first star in the Universe are rather simple: (i) The chemical and radiative processes in the primordial gas are readily understood. (ii) Strong magnetic fields are not expected to exist at early times. (iii) By definition, no other stars exist to influence the environment through radiation, winds, supernovae, etc. (iv) The emerging standard model for structure formation provides appropriate initial conditions.

In previous work, we have presented three-dimensional (3D) cosmological simulations of the formation of the first objects in the Universe (*5, 6*), including the first applications of adaptive mesh refinement (AMR) cosmological hydrodynamical simulations to first structure formation (*7, 8*). In these studies we achieved a dynamic range (ratio of the side length of the simulation volume to the side length of the smallest resolution element) of up to 2×10^5 and could follow in detail the formation of the first dense cooling region far within a pregalactic object that formed self-consistently from linear density fluctuation in a cold dark matter (CDM) cosmology. Here, we report results from simulations that extend our previous work by another five orders of magnitude in dynamic range, enabling us to bridge the wide range between cosmological and stellar scale.

[1]Harvard Smithsonian Center for Astrophysics, Cambridge, MA 02138, USA. [2]Institute of Astronomy, University of Cambridge, Cambridge CB3 0HA, UK. [3]Astrophysics Division, Department of Physics, Massachusetts Institute of Technology, Cambridge, MA 02139, USA. [4]Center for Astrophysics & Space Sciences, University of California, San Diego, La Jolla, CA 92093, USA.

Simulation setup and numerical issues. We use an Eulerian structured AMR cosmological hydrodynamical code developed by Bryan and Norman (*9, 10*). The hydrodynamical equations are solved with the second-order accurate piecewise parabolic method (*11, 12*) where a Riemann solver ensures accurate shock capturing with a minimum of numerical viscosity. We use initial conditions appropriate for a spatially flat CDM cosmology with 6% of the matter density contributed by baryons, zero cosmological constant, and a Hubble constant of 50 km s^{-1} Mpc^{-1} (*13*). The power spectra of initial density fluctuations in the dark matter and the gas are taken from the computation by the publicly available Boltzmann code CMBFAST (*14*) at redshift 100 (assuming a Harrison-Zel'dovich scale-invariant initial spectrum).

We set up a 3D volume with 128 kpc on a side (co-moving) and solve the cosmological hydrodynamics equations assuming periodic boundary conditions. This small volume is adequate for our purpose, because we are interested in the evolution of the first pregalactic object within which a star may be formed by a redshift of $z \sim 20$. First, we identify the Lagrangian volume of the first protogalactic halo with a mass of $\sim10^6$ $M_\odot$ in a low-resolution pure N-body simulation. Then we generate new initial conditions with four initial static grids that cover this Lagrangian region with progressively finer resolution. With a 64^3 top grid and a refinement factor of 2, this specifies the initial conditions in the region of interest equivalent to a 512^3 uni-grid calculation. For the adopted cosmology, this gives a mass resolution of 1.1 $M_\odot$ for the dark matter (DM hereafter) and 0.07 $M_\odot$ for the gas. The small DM masses ensure that the cosmological Jeans mass is resolved by at least 10,000 particles at all times. Smaller scale structures in the DM will not be able to influence the baryons because of their shallow potential wells. The theoretical expectation holds, because the simulations of (*8*), which had poorer DM resolution by a factor of 8, led to results on large scales identical to those of the simulation presented here.

During the evolution, refined grids are introduced with twice the spatial resolution of the parent (coarser) grid. These child (finer) meshes are added whenever one of three refinement criteria are met. Two Lagrangian criteria ensure that the grid is refined whenever the gas (or DM) density exceeds its initial density by a factor of 4.6 (or 9.2). Additionally, the local Jeans length is always covered by at least 64 grid cells (*15*) [four cells per Jeans length would be sufficient (*16*)]. We have also carried out the simulations with identical initial conditions but varying the refinement criteria. In one series of runs, we varied the number of mesh points per Jeans length. Runs with 4, 16, and 64 zones per Jeans length are indistinguishable in all mass-weighted radial profiles of physical quantities. No change in the angular momentum profiles could be found, suggesting negligible numerical viscosity effects on angular momentum transport. A further refinement criterion that ensured the local cooling time scale to be longer than the local Courant time also gave identical results. This latter test checked that any thermally unstable region was identified.

The simulation follows the nonequilibrium chemistry of the dominant nine species (H, H^+, H^-, e^-, He, He^+, He^{2+}, H_2, and H_2^+) in primordial gas. Furthermore, the radiative losses from atomic and molecular line cooling, Compton cooling, and heating of free electrons by the cosmic background radiation are appropriately treated in the optically thin limit (*17, 18*). To extend our previous studies to higher densities, we made three essential modifications to the code. First, we implemented the three-body molecular hydrogen formation process k_{3b} ($H + H + H \rightarrow H_2 + H$) in the chemical rate equations. For temperatures below 300 K, we fit to the data of Orel (*19*) to get $k_{3b} = 1.3 \times 10^{-32}(T/300\ \mathrm{K})^{-0.38}\ \mathrm{cm}^6\ \mathrm{s}^{-1}$. Above 300 K, we then matched k_{3b} continuously to a power law (*4*), $k_{3b} = 1.3 \times 10^{-32}(T/300\ \mathrm{K})^{-1}\ \mathrm{cm}^6\ \mathrm{s}^{-1}$. Second, we introduced a variable adiabatic index for the gas (*20*). The dissipative component (baryons) may collapse to much higher densities than the collisionless component (DM). Third, we smoothed the DM particles with a Gaussian of width 0.05 pc for grids with cells smaller than this length. This smoothing is done to avoid artificial heating of the baryons (cooling for the DM) once the gas density becomes much larger than the local DM density because of the discrete sampling of the DM potential by particles. At this scale, the enclosed gas mass substantially exceeds the enclosed DM mass and hence dominates the potential.

The standard message passing library (MPI) was used to implement domain decomposition on the individual levels of the grid hierarchy as a parallelization strategy. The code was run in parallel on 16 processors of the SGI Origin2000 supercomputer at the National Center for Supercomputing Applications at the University of Illinois at Urbana-Champaign.

We stop the simulation at a time when the molecular cooling lines reach an optical depth of 10 at line center because our numerical method cannot treat the difficult problem of time-dependent radiative line transfer in multiple dimensions. At this time, the code uses >5500 grids on 27 refinement levels with $1.8 \times 10^7 \approx 260^3$ computational grid cells. An average grid therefore contains $\sim 15^3$ cells.

Characteristic mass scales. Our simulations (Figs. 1 and 2) identify at least four characteristic mass scales. From the outside going in, one observes infall and accretion onto the pregalactic halo with a total mass of $7 \times 10^5\ M_\odot$, consistent with previous studies [see (*5, 6, 8, 21, 22*) for discussion and references].

At a mass scale of about 4000 $M_\odot$ ($r \sim 10$ pc), rapid cooling and infall is observed. This is accompanied by the first of three valleys in the radial velocity distribution (Fig. 2E). The temperature drops and the molecular hydrogen fraction increases. It is here, at number densities of $\sim 10\ \mathrm{cm}^{-3}$, that the high-redshift analog of a molecular cloud is formed. Although the molecular mass fraction is not even 0.1%, it is sufficient to cool the gas rapidly down to ~200 K. The gas cannot cool

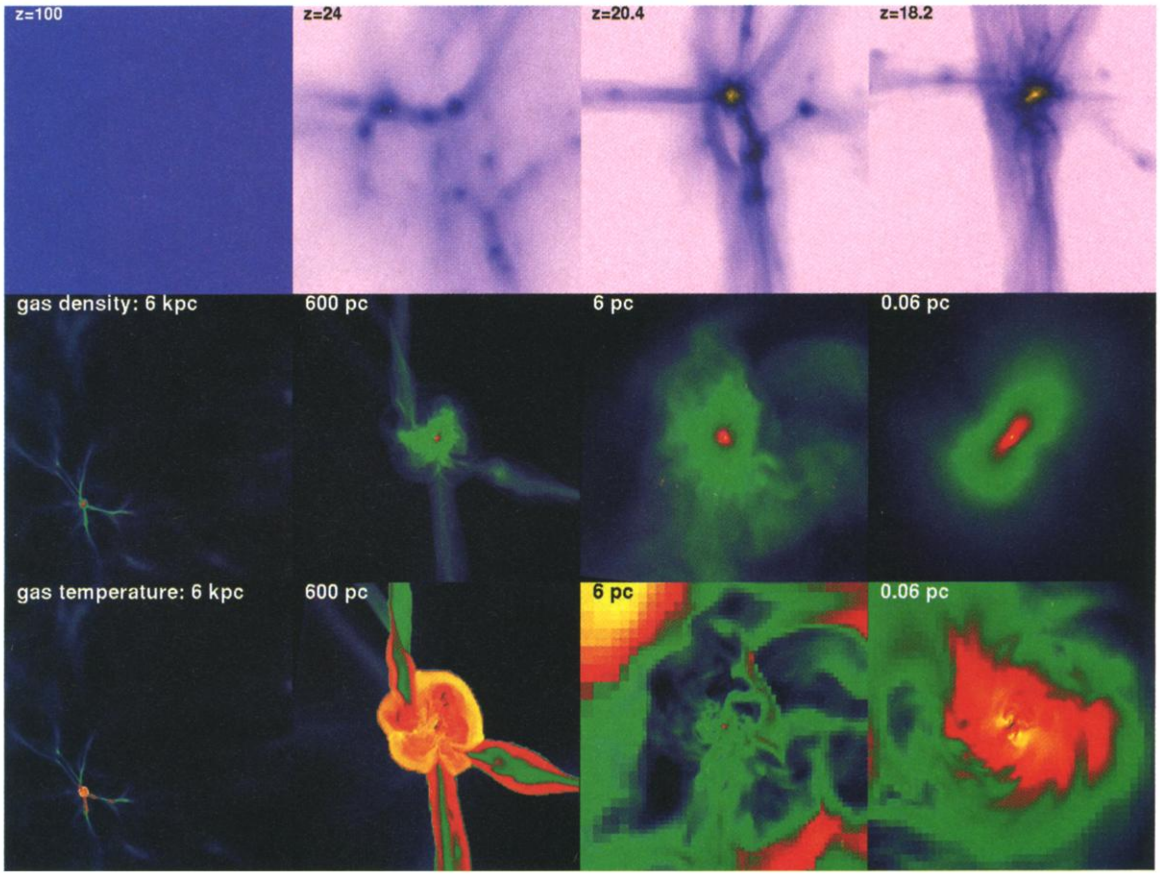

Fig. 1. Overview of the evolution and collapse forming a primordial star in the Universe. The top row shows projections of the gas density of one-thousandth of the simulation volume approximately centered at the pregalactic object within which the star is formed. The four projections from left to right are taken at redshifts 100, 24, 20.4, and 18.2, respectively. The pregalactic objects form from very small density fluctuations and continuously merge to form larger objects. The middle and bottom rows show thin slices through the gas density and temperature at the final simulation output. The leftmost panels are on the scale of the simulation volume, ~6 kpc (proper) (*45*). The panels to the right zoom in toward the forming star and have side lengths of 600 pc, 6 pc, and 0.06 pc (12,000 astronomical units). The color maps (going from black to blue, green, red, and yellow) are logarithmic, and the associated values were adjusted considerably to visualize the ~17 orders of magnitude in density covered by these simulations. In the left panels, the larger scale structures of filaments and sheets are seen. At their intersections, a pregalactic object of $\sim 10^6\ M_\odot$ is formed. The temperature slice (second panel, bottom row) shows how the gas shock heats as it falls into the pregalactic object. After passing the accretion shock, the material forms hydrogen molecules and starts to cool. The cooling material accumulates at the center of the object and forms the high-redshift molecular cloud analog (third panel from the right), which is dense and cold ($T \sim 200$ K). Deep within the molecular cloud, a core of ~100 $M_\odot$, a few hundred K warmer, is formed (right panel) within which a 1 $M_\odot$ protostar is formed (yellow region in the right panel of the middle row).

below this temperature because of the sharp decrease in the cooling rate below ~200 K.

At redshift 19 (Fig. 2), there are only two mass scales; however, as time passes the central density grows and eventually passes 10^4 cm^{-3}, at which point the ro-vibrational levels of H_2 are populated at their equilibrium values and the cooling time becomes independent of density (instead of inversely proportional to it). This reduced cooling efficiency leads to an increase in the temperature (Fig. 2D). As the temperature rises, the cooling rate again increases (it is 1000 times as fast at 800 K as at 200 K) and the inflow velocities slowly climb.

To better understand what happens next, we examine the stability of an isothermal gas sphere. The critical mass for gravitational collapse given an external pressure P_{ext} (BE mass hereafter) is given by Ebert (*23*) and Bonnor (*24*) as

$$M_{BE} = 1.18\, M_{\odot}(c_s^4/G^{3/2})P_{ext}^{-1/2}$$

$$c_s^2 = dP/d\rho = \gamma k_B T/\mu m_H \qquad (1)$$

where T is the gas temperature, ρ is mass density, m_H is the proton mass, and G, k_B, and c_s are the gravitational constant, the Boltzmann constant, and the sound speed, respectively. We can estimate this critical mass locally if we set the external pressure to be the local pressure to find $M_{BE} \approx 20\, M_{\odot}\, T^{3/2} n^{-1/2} \mu^{-2} \gamma^2$ where n is the particle number density and $\mu \approx 1.22$ is the mean mass per particle in units of the proton mass. Using an adiabatic index $\gamma = 5/3$, we plot the ratio of the enclosed gas mass to this modified BE mass in Fig. 3.

Our modeling (Fig. 3) shows that by the fourth considered output time, the central 100 $M_{\odot}$ exceeds the BE mass at that radius, indicating unstable collapse. This is the third mass scale and corresponds to the second local minimum in the radial velocity curves (Fig. 2E). The inflow velocity, 1 km s^{-1}, is still subsonic. Although this mass scale is unstable, it does not represent the smallest scale of collapse in our simulation. This is due to the increasing molecular hydrogen fraction.

When the gas density becomes sufficiently large (~10^{10} cm^{-3}), three-body molecular hydrogen formation becomes important. This rapidly increases the molecular fraction (Fig. 2C) and hence the cooling rate. The increased cooling leads to lower temperatures and even stronger inflow. At a mass scale of ~1 $M_{\odot}$, not only is the gas nearly completely molecular, but the radial inflow has become supersonic (Fig. 2E). When the H_2 mass fraction approaches unity, the increase in the cooling rate saturates, and the gas goes through a radiative shock. This marks the first appearance of the protostellar accretion shock at a radius of about 20 astronomical units from its center.

Chemothermal instability. When the cooling time becomes independent of density, the classical criterion for fragmentation $t_{cool} < t_{dyn} \propto n^{-1/2}$ (*25*) cannot be satisfied at high densities. However, in principle the medium may still be subject to thermal instability. The instability criterion is

$$\rho(\partial L/\partial\rho)_{T=\text{const.}} - T(\partial L/\partial T)_{\rho=\text{const.}} + L(\rho,T) > 0 \qquad (2)$$

where L denotes the cooling losses per second of a fluid parcel. At densities above the critical densities of molecular hydrogen, the cooling time is independent of density; that is, $\partial L/\partial\rho = \Lambda(T)$, where $\Lambda(T)$ is the high-density cooling function [e.g., (*26*)]. Fitting the cooling function with a power law locally around a temperature T_0 [so that $\Lambda(T) \propto (T/T_0)^{\alpha}$] yields $\partial L/\partial T = \rho\alpha\Lambda(T)/T$. Hence, under these circumstances the medium is

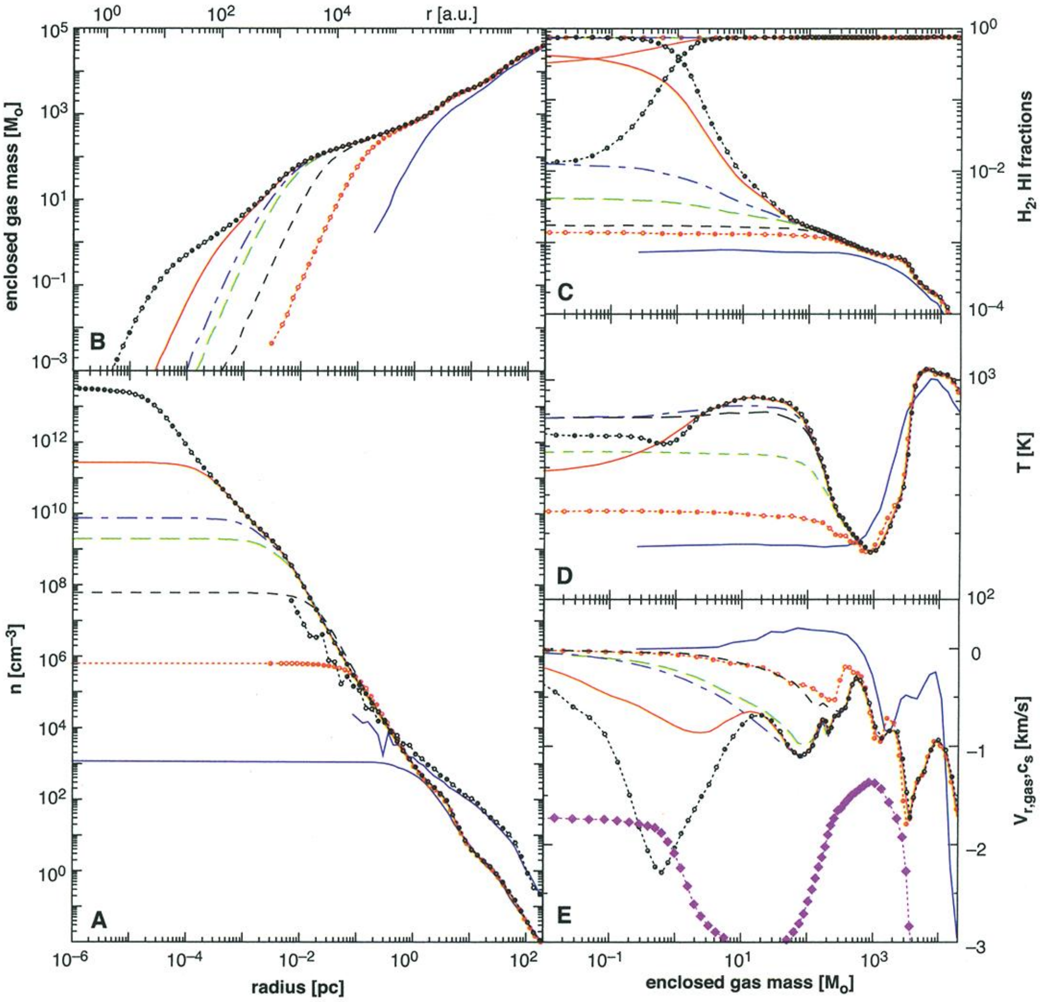

Fig. 2. Radial mass-weighted averages of various physical quantities at seven different output times. (**A**) Evolution of the particle number density in cm^{-3} as a function of radius at redshift 19 (purple solid line), 9 million years later (red dotted lines with circles), 300,000 years later (black dashed line), 30,000 years later (green long-dashed line), 3000 years later (purple dot-dashed line), 1500 years later (red solid line), and 200 years later (black dotted line with circles) at $z = 18.181164$. The two lines between 10^{-2} and 200 pc give the DM mass density in GeV cm^{-3} at $z = 19$ and the final time, respectively. (**B**) Enclosed gas mass as a function of radius. (**C**) Mass fractions of atomic hydrogen and molecular hydrogen. (**D** and **E**) Temperature evolution and the mass-weighted radial velocity of the baryons, respectively. The bottom line with solid symbols in (E) shows the negative value of the local speed of sound at the final time. In all panels the same output times correspond to the same line styles.

thermally stable if $\alpha > 2$. Because $\alpha > 4$ for the densities and temperatures of interest, we conclude that the medium is thermally stable. The above analysis neglects the heating from contraction, but this only strengthens the conclusion. If heating balances cooling, one can neglect the $+L(\rho,T)$ term in Eq. 2 and find the medium to be thermally stable for $\alpha > 1$.

However, here we neglected the chemical processes. The detailed analysis for the case when chemical processes occur on the time scale of the collapse is well known (*27*) and can be applied to primordial star formation (*28*), including the three-body formation of molecular hydrogen (*4*), which drives a chemothermal instability. Evaluation of all the terms in this modified instability criterion [(*28*), equation 36] shows that for molecular mass fractions $f < 6/(2\alpha + 1)$, the medium is expected to be chemothermally unstable. These large molecular fractions show that the strong density dependence of the three-body H_2 formation dominates the instability. Upon examination of the 3D temperature and H_2 density field, we clearly see this chemothermal instability at work. Cooler regions have larger H_2 fractions. However, no correspondingly large density inhomogeneities are found and fragmentation does not occur. This happens because of the short sound crossing times in the collapsing core. When the H_2 formation time scale becomes shorter than the cooling time, the instability originates. However, as long as the sound crossing time is much shorter than the chemical and cooling time scales, the cooler parts are efficiently mixed with the warmer material. This holds in our simulation until the final output, where for the first time the H_2 formation time scale becomes shorter than the sound crossing time. However, at this point the protostellar core is fully molecular and stable against the chemothermal instability. Consequently, no large density contrasts are formed. Because at these high densities the optical depth of the cooling radiation becomes larger than unity, the instability will be suppressed even further.

Angular momentum. Interestingly, rotational support does not halt the collapse, for two reasons. The first is shown in Fig. 4A, which plots the specific angular momentum against enclosed mass for the same seven output times discussed earlier. For the first output time (Fig. 4), we see that the central gas begins the collapse with a specific angular momentum only ~0.1% as large as the mean value. This type of angular momentum profile is typical of halos produced by gravitational collapse [e.g., (*29*)] and means that the protostellar gas starts out with little angular momentum to lose. As a graphic example of this phenomenon, consider the central solar mass of the collapsing region. It has only an order of magnitude less angular momentum at densities $n \sim >10^{13}$ cm^{-3} than it had at $n \sim >10^6$ cm^{-3}, although it collapsed by a factor of >100 in radius.

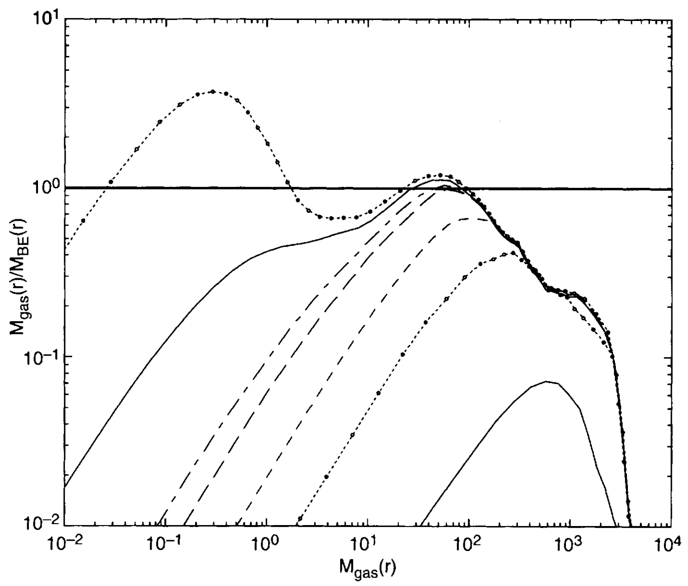

Fig. 3. Ratio of enclosed gas mass to the locally estimated Bonnor-Ebert mass ($M_{BE} \approx 61\ M_\odot T_K^{3/2} n^{-1/2} \mu^{-2}$) for various output times. The enclosed gas mass exceeds the BE mass at two different mass scales, ~1 $M_\odot$ and ~100 $M_\odot$. The line styles correspond to the output times shown in Fig. 2.

The second reason why rotation does not halt the collapse is that angular momentum is transported. This transport is clearly seen (Fig. 4) in the central 100 $M_\odot$ in the last five illustrated output times (because L plotted as a function of enclosed mass should stay constant as long as there is no shell crossing). In Fig. 4C, we divide L by r to get a typical rotational velocity, and in Fig. 4, B and D, we compare this velocity to the Keplerian rotational velocity and the local sound speed, respectively.

We find that the typical rotational speed is below that required for rotational support by a factor of 2 to 3. Furthermore, we see that this azimuthal speed never rises much above the sound speed, although for most of the mass below 100 $M_\odot$ it is comparable in value. We interpret this as evidence that shock waves during the turbulent collapse are responsible for much of the transported angular momentum. A collapsing turbulent medium is different from a disk in Keplerian rotation. At any radius, there will be both low and high angular momentum material, and pressure forces or shock waves can redistribute the angular momentum between fluid elements. Lower angular momentum material will selectively sink inward, displacing higher angular momentum gas. This hydrodynamic transport of angular momentum will be suppressed in situations where the collapse proceeds on the dynamical time rather on the longer cooling time, as in the presented case. This difference in cooling time and the widely different initial conditions may explain why this mechanism has not been observed in simulations of present-day star formation [e.g., (*30*) and references therein]. However, such situations may also arise in the late stages of the formation of present-day stars and in scenarios for the formation of supermassive black holes.

To ensure that the angular momentum transport cannot be attributed to numerical shear viscosity (*31*), we have carried out the resolution study discussed above. We have varied the effective spatial resolution by a factor of 16 and found identical results. Moreover, we have run the AMR code with two different implementations of the hydrodynamics solver. The resolution study and the results presented here were carried out with a direct piecewise parabolic method adopted for cosmology (*11, 12*). We ran another simulation with the lower order ZEUS hydrodynamics (*32*) and still found no relevant differences. These tests are not strict proof that the encountered angular momentum transport is not caused by numerical effects, but they are reassuring.

Magnetic fields? The strength of magnetic fields generated around the epoch of recombination is minute. In contrast, phase transitions at the quantum chromodynamic (QCD) and electro-weak scales may form dynamically important fields. Although there are many such scenarios for primordial magnetic field generation in the early Universe, they are not considered to be an integral part of our standard picture of structure formation. This is because not even the order of these phase transitions is known [(*33*) and references therein]. Unfortunately, strong primordial small-scale ($\ll$1 Mpc, co-moving) magnetic fields are poorly constrained observationally (*34*).

The critical magnetic field for support of a cloud (*35*) allows one to estimate how strong a primordial magnetic field would have to be in order to influence our simulation results. For this we also assume a flux-frozen flow with no additional amplification of the magnetic field other than the contraction ($B \propto \rho^{2/3}$). For a co-moving B field of $\sim >3 \times$

Fig. 4. Radial mass-weighted averages of various physical quantities related to the angular momentum of the gas. The seven different output times correspond to those described in Fig. 2. (**A**) The specific angular momentum L as a function of enclosed gas mass. (**C**) The typical rotational speed L/r. (**B** and **D**) The ratio of L/r to the Keplerian velocity $V_{\mathrm{Kepler}} = (GM/r)^{1/2}$ and the local speed of sound c_s, respectively.

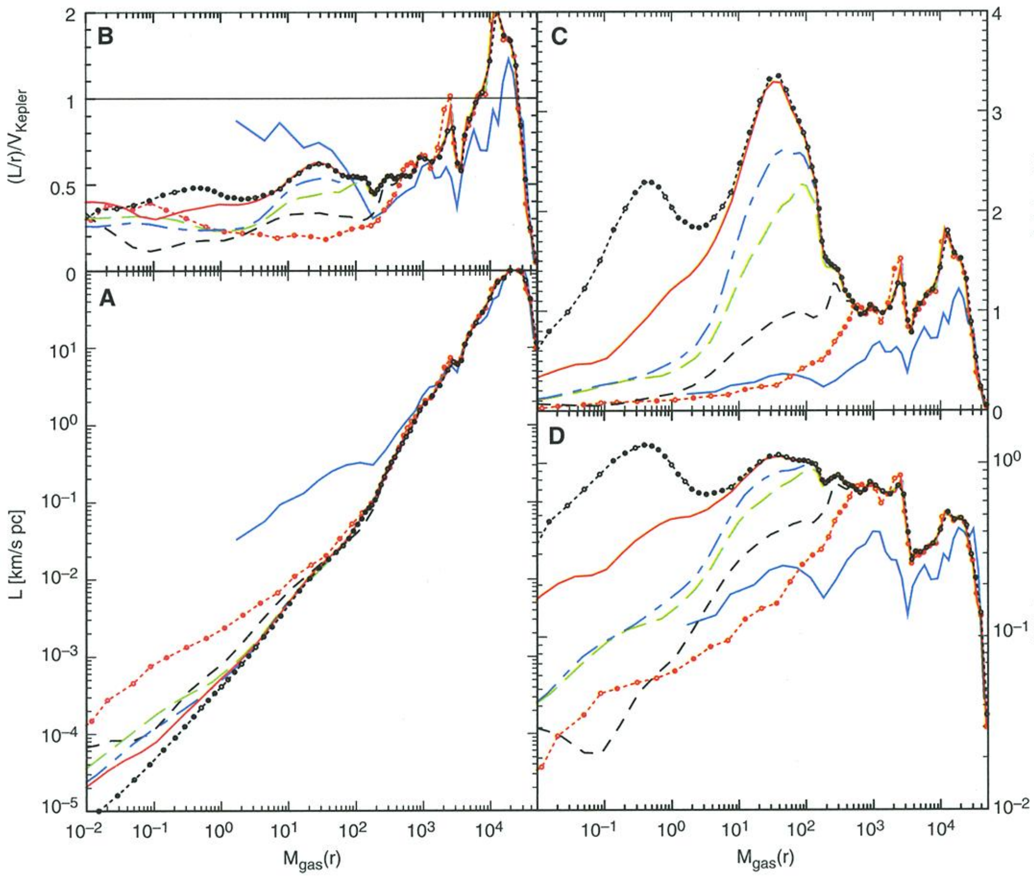

10^{-11} G on scales of $\sim <100$ kpc, the critical field needed for support may be reached during the collapse, possibly modifying the mass scales found in our purely hydrodynamic simulations. However, the ionized fraction drops rapidly during the collapse because of the absence of cosmic ray ionization. Consequently, ambipolar diffusion should be much more effective in the formation of the first stars even if such strong primordial magnetic fields were present.

Discussion. Previously we discussed the formation of the pregalactic object and the primordial "molecular cloud" that hosts the formation of the first star in the simulated patch of the Universe (*8*). These simulations had a dynamic range of $\sim 10^5$ and identified a $\sim 100\ M_\odot$ core within the primordial "molecular cloud" undergoing renewed gravitational collapse. The fate of this core was unclear because of the potential caveat that three-body H_2 formation could have caused fragmentation. Indeed, this further fragmentation had been suggested by analytic work (*28*) and single-zone models (*4*). The 3D simulations described here were designed to test whether the three-body process will lead to a breakup of the core. No fragmentation due to three-body H_2 formation was found. This is in large part because of the slow quasi-hydrostatic contraction found in (*8*), which allows subsonic damping of density perturbations and yields a smooth distribution at the time when three-body H_2 formation becomes important. Instead of fragmentation, a single fully molecular protostar of $\sim 1\ M_\odot$ is formed at the center of the $\sim 100\ M_\odot$ core.

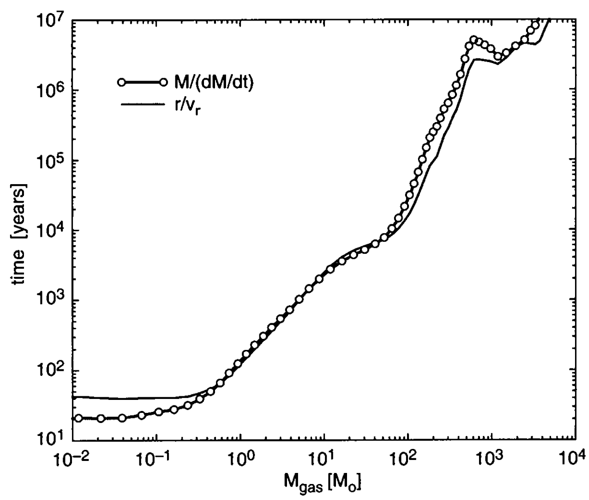

Fig. 5. Accretion time as function of enclosed gas mass. The line with symbols gives $M(r)/[4\pi\rho(r)r^2|v_r(r)|]$, where v_r is the radial velocity of the gas. The solid line simply shows how long it would take the mass to move to $r = 0$ if it were to keep its current radial velocity $[r/v_r(M)]$.

However, even with extraordinary resolution, the final mass of the first star remains unclear. Whether all the available cooled material of the surroundings will accrete onto the protostar, or whether feedback from the forming star will limit further accretion (and hence its own growth), is difficult to compute in detail.

Within 10^4 years, about 70 $M_\odot$ may be accreted, assuming that angular momentum will not slow the collapse (Fig. 5). The maximum of the accretion time of $\sim 5 \times 10^6$ years is at $\sim 600\ M_\odot$. However, stars larger than 100 $M_\odot$ will explode within ~ 2 million years. Therefore, it seems unlikely (even in the absence of angular momentum) that there would be sufficient time to accrete such large masses.

A 1 $M_\odot$ protostar will evolve too slowly to halt substantial accretion. From the accretion time profile (Fig. 5), one may argue that a more realistic minimum mass limit of the first star should be ~>30 $M_\odot$ because this amount would be accreted within a few thousand years. This is a very short time relative to expected protostellar evolution times. However, some properties of the primordial gas may make it easier to halt the accretion. One possibility is the destruction of the cooling agent, molecular hydrogen, without which the accreting material may reach hydrostatic equilibrium. This may or may not be sufficient to halt the accretion. Another possible scenario is that the central material heats up to 10^4 K, allowing Lyman-α cooling from neutral hydrogen. That cooling region may expand rapidly as the internal pressure drops because of infall, possibly allowing the envelope to accrete even without molecular hydrogen as the cooling agent. Additionally, radiation pressure from ionizing photons as well as atomic hydrogen Lyman series photons may become important and eventually reverse the flow. The mechanisms discussed by Haehnelt (*36*) on galactic scales will play an important role for the continued accretion onto the protostar. This is an interplay of many complex physical processes, because the situation can be construed as a hot ionized Strömgren sphere through which cool and dense material is trying to accrete. In such a situation, one expects a Raleigh-Taylor type instability that is modified via the geometry of the radiation field.

At the final output time presented here, there are $\sim 4 \times 10^{57}$ hydrogen molecules in the entire protogalaxy. Also, the H_2 formation time scale is long because there are no dust grains and the free electrons (needed as a catalyst) have almost fully recombined. Hence, as soon as the first ultraviolet photons of Lyman Werner band frequencies are produced, a rapidly expanding photodissociating region will inhibit further cooling within it. This photodissociation will prevent further fragmentation at the molecular cloud scale (i.e., no other star can be formed within the same halo before the first star dies in a supernova). The supernova may have sufficient energy to unbind the entire gas content of the small pregalactic object it formed in (*37*). This will have interesting consequences for the dispersal of metals, entropy, and magnetic field into the intergalactic medium (*38, 39*).

Smoothed particle hydrodynamics (SPH) [e.g., (*40*)], used extensively in cosmological hydrodynamics, can also be used (*22*) to follow the collapse of solid-body rotating uniform spheres. The assumption of coherent rotation causes these clouds to collapse into a disk that develops filamentary structures, which eventually fragment to form dense clumps of masses between 100 and $1000 M_\odot$. It has been argued that these clumps will continue to accrete and merge, and eventually will form very massive stars. These SPH simulations have unrealistic initial conditions and much lower resolution than our calculations. However, they also show that many details of the collapse forming a primordial star are determined by the properties of the hydrogen molecule.

We have also simulated different initial density fields for a flat CDM cosmology with a cosmological constant $\Omega(\Lambda) = 0.7$. In that study, we focused on halos with different clustering environments. Although we have not followed the collapse in these halos to protostellar densities, we have found no qualitative differences in the "primordial molecular cloud" formation process as discussed in (*8*). Also, other AMR simulations (*41*) give consistent results on scales larger than 1 pc. In all cases a cooling flow forms the primordial molecular cloud at the center of the DM halo. We conclude that the molecular cloud formation process seems to be independent of the halo clustering properties and the adopted CDM-type cosmology. Also, the mass scales for the core and the protostar are determined by the local Bonnor-Ebert mass. Consequently, we expect the key results discussed here to be insensitive to variations in cosmology or halo clustering.

The picture arising from these numerical simulations has some interesting implications. It is possible that all metal-free stars are massive and form in isolation. Their supernovae may provide the metals seen in even the lowest column density quasar absorption lines [(*1*) and references therein]. Massive primordial stars offer a natural explanation for the absence of purely metal-free low-mass stars in the Milky Way. The consequences for the formation of galaxies may be even more profound in that the supernovae provide metals, entropy, and magnetic fields and may even alter the initial power spectrum of density fluctuations of the baryons.

Interestingly, it has been recently argued, from abundance patterns, that galactic halo stars of low metallicity seem to have been enriched by only one population of massive stars (*42*). These results, if confirmed, would represent strong support for the picture arising from our ab initio simulations of first structure formation.

There is suggestive evidence that links gamma ray bursts to sites of massive star formation [e.g., (*43*)]. It would be very fortunate if a large fraction of the massive stars naturally formed in the simulations would cause gamma ray bursts [e.g., (*44*)]. Such high-redshift bursts would open a remarkably bright window for the study of the otherwise dark (faint) ages.

References and Notes

1. S. L. Ellison, A. Songaila, J. Schaye, M. Pettini, *Astron. J.* **120**, 1175 (2000).
2. P. J. E. Peebles, R. H. Dicke, *Astrophys. J.* **154**, 891 (1968).
3. T. Hirasawa, *Prog. Theor. Phys.* **42**, 523 (1969).
4. F. Palla, E. E. Salpeter, S. W. Stahler, *Astrophys. J.* **271**, 632 (1983).
5. T. Abel, thesis, University of Regensburg, Germany (1995).
6. ———, P. Anninos, M. L. Norman, Y. Zhang, *Astrophys. J.* **508**, 518 (1998).
7. T. Abel, G. L. Bryan, M. L. Norman, in *Evolution of Large Scale Structure: From Recombination to Garching*, T. Banday, R. K. Sheth, L. N. Da Costa, Eds. (European Southern Observatory, Garching, Germany, 1999), p. 363.
8. ———, *Astrophys. J.* **540**, 39 (2000).
9. G. L. Bryan, M. L. Norman, in *Computational Astrophysics*, D. A. Clarke, M. Fall, Eds. (ASP Conference Series 123, Astronomical Society of the Pacific, San Francisco, 1997), p. 363.
10. ———, in *Workshop on Structured Adaptive Mesh Refinement Grid Methods*, N. Chrisochoides, Ed. (IMA Volumes in Mathematics No. 117, Springer-Verlag, New York, 1999), p. 165.
11. P. R. Woodward, P. Colella, *J. Comput. Phys.* **54**, 115 (1984).
12. G. L. Bryan, R. Cen, M. L. Norman, J. P. Ostriker, J. M. Stone, *Astrophys. J.* **428**, 405 (1994).
13. Friedmann models with a cosmological constant, which currently seem to fit various observational tests better, differ from the standard CDM model considered here only slightly at the high redshifts modeled.
14. U. Seljak, M. Zaldarriaga, *Astrophys. J.* **469**, 437 (1996).
15. The Jeans mass, which is the relevant mass scale for collapse and fragmentation, is thus resolved by at least $4\pi 32^3/3 \approx 1.4 \times 10^5$ cells.
16. J. K. Truelove *et al.*, *Astrophys. J.* **489**, L179 (1997).
17. T. Abel, P. Anninos, Y. Zhang, M. L. Norman, *New Astron.* **2**, 181 (1997).
18. P. Anninos, Y. Zhang, T. Abel, M. L. Norman, *New Astron.* **2**, 209 (1997).
19. A. E. Orel, *J. Chem. Phys.* **87**, 314 (1987).
20. K. Omukai, R. Nishi, *Astrophys. J.* **508**, 141 (1998).
21. M. Tegmark *et al.*, *Astrophys. J.* **474**, 1 (1997).
22. V. Bromm, P. S. Coppi, R. B. Larson, *Astrophys. J.* **527**, L5 (1999).
23. R. Ebert, *Z. Astrophys.* **37**, 217 (1955).
24. W. B. Bonnor, *Mon. Not. R. Astron. Soc.* **116**, 351 (1956).
25. G. B. Field, *Astrophys. J.* **142**, 531 (1965).
26. D. Galli, F. Palla, *Astron. Astrophys.* **335**, 403 (1998).
27. Y. Sabano, Y. Yoshi, *Publ. Astron. Soc. Jpn.* **29**, 207 (1977).
28. J. Silk, *Mon. Not. R. Astron. Soc.* **205**, 705 (1983).
29. P. J. Quinn, W. H. Zurek, *Astrophys. J.* **331**, 1 (1988).
30. A. Burkert, P. Bodenheimer, *Mon. Not. R. Astron. Soc.* **264**, 798 (1993).
31. M. L. Norman, J. R. Wilson, R. T. Barton, *Astrophys. J.* **239**, 968 (1980).
32. J. M. Stone, M. L. Norman, *Astrophys. J. Suppl. Ser.* **80**, 791 (1992).
33. G. Sigl, A. V. Olinto, K. Jedamzik, *Phys. Rev. D* **55**, 4582 (1997).
34. J. D. Barrow, P. G. Ferreira, J. Silk, *Phys. Rev. Lett.* **78**, 3610 (1997).
35. T. Ch. Mouschovias, L. Spitzer, *Astrophys. J.* **210**, 326 (1976).
36. M. G. Haehnelt, *Mon. Not. R. Astron. Soc.* **273**, 249 (1995).
37. M. Mac Low, A. Ferrara, *Astrophys. J.* **513**, 142 (1999).
38. A. Ferrara, *Astrophys. J.* **499**, L17 (1998).
39. R. Cen, G. L. Bryan, *Astrophys. J.* **546**, L81 (2000).
40. J. J. Monaghan, *Annu. Rev. Astron. Astrophys.* **30**, 543 (1992).
41. M. E. Machacek, G. L. Bryan, T. Abel, *Astrophys. J.* **548**, 509 (2001).
42. G. J. Wasserburg, Y. Qian, *Astrophys. J.* **529**, L21 (2000).
43. D. E. Reichart, *Astrophys. J.* **521**, L111 (1999).
44. B. Ciardi, A. Loeb, *Astrophys. J.* **540**, 687 (2000).
45. A co-moving length scale is $(1 + z)$ times the proper length, where z is the cosmological redshift; that is, 1 kpc (proper) at redshift 9 is equal to 10 kpc (co-moving).

46. T.A. thanks M. Rees and R. Larson for stimulating and insightful discussions. Supported by Hubble Fellowship grant HF-0110401-98A from the Space Telescope Science Institute, which is operated by the Association of Universities for Research in Astronomy Inc. under NASA contract NAS5-26555 (G.L.B.).

2 July 2001; accepted 31 October 2001
Published online 15 November 2001;
10.1126/science.1063991
Include this information when citing this paper.